Polymer Testing 113 (2022) 107647

Contents lists available at ScienceDirect

Polymer Testing

journal homepage: www.elsevier.com/locate/polytest

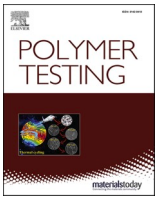

# Selective recovery of lithium resources in salt lakes by polyacrylonitrile/ion-imprinted polymer: Synthesis, testing, and computation

Tao Ding [a], Qian Wu [b,*], Zhen Nie [b,**], Mianping Zheng [b], Yunsheng Wang [b], Donghui Yang [c]

[a] College of Geoscience and Surveying Engineering, China University of Mining and Technology, (Beijing), Beijing, 100083, China
[b] MNR Key Laboratory of Saline Lake Resources and Environments, Institute of Mineral Resources, Chinese Academy of Geological Sciences, Beijing, 100037, China
[c] Hebei Earthquake Agency the Central Station of Chengde Earthquake Observation and Measurement, Chengde, 067000, China

ARTICLE INFO

*Keywords:*
Ion-imprinted polymer
Nanofiber
Li(I) adsorption
Density functional theory
Salt-lake brine

ABSTRACT

Lithium as a strategic metal exhibits extensive applications in the 21st century. The high-efficiency extraction of lithium resources is of economic significance as the market demand for electric vehicles powered by lithium-ion batteries increases rapidly. A novel silica gel (SG)/graphene oxide (GO) composite nanofiber was prepared by combining surface imprinting technology with electrospinning technology to capture Li(I) from salt lakes in an oriented manner. The batch adsorption experiments and fixed-bed adsorption experiments were conducted to evaluate the adsorption performance of the composites. The SG/GO composite exhibited a maximum adsorption capacity of 1.1 mg/g for Li(I). The adsorption kinetics tallied with the pseudo-second-order model, and the isothermal adsorption was similar to the Langmuir model. The adsorption process of the SG/GO composite is one of monolayer chemical adsorption, and the adsorbates did not interact. The adsorption mechanism was revealed by Fourier transform infrared (FT-IR) spectroscopy and scanning electron microscopy (SEM), combined with density functional theory (DFT) computation. The mechanism analysis indicated that the charge transfer occurred between the surface functional groups and metal ions in the adsorption process. The electrons mainly transferred from the P and O atoms of the functional groups to the 3p orbit of Li(I) to form coordinate bonds, which finally achieved the goal of oriented capture of Li(I). The polyacrylonitrile (PAN)/ion-imprinted polymer (IIP) composite nanofiber is a novel, high-efficiency adsorbing material for recovering Li(I) from salt-lake brine.

## 1. Introduction

Lithium as the lightest alkali metal is an important strategic resource in the 21st century [1–3], which is widely applied in the fields of glass [4], nuclear reactors [5,6], and lithium batteries [7–10]. In recent years, the market price of lithium is rising apace due to the rapid development of new energy vehicles [11], and the demand for lithium resources is also growing constantly at a rate of 10% per year [12]. There is about 70% of global lithium resources in the salt lakes [13]. Therefore, it is important to realize the selective extraction of lithium resources from the salt-lake brine to alleviate the supply shortage of lithium resources in the market.

Our research team is dedicated to studying the recovery of lithium resources from the salt-lake brine in China since 2000. The salinity gradient solar pond method was pioneered to recover the lithium resources from Zabuye Salt Lake in the Tibet Autonomous Region of China, which is the first production base for extracting lithium from salt lakes and is still in use [14–19]. However, the construction of salt pans requires a long processing cycle. New attempts were made, as described in this paper. At present, a variety of Li(I) recovery technologies were reported [20–22], including solvent extraction method [23–26], membrane separation technique [27–31], precipitation method [32], and adsorption method [33–36]. Among them, the adsorption method is regarded as one of the most promising to extract Li(I) from the salt-lake brine, which is benefit from its unique advantages such as simple production process, low cost, controllable extraction process, and low energy consumption [37,38]. Researchers employed $TiO_2$ or $Ti(OC_4H_9)_4$ as the titanium sources and LiOH, $Li_2CO_3$, or $CH_3COOLi$ as the lithium sources to produce the precursors through the combination of the high-temperature solid-state method, hydrothermal synthesis, and sol-gel technique. The pre-introduced Li(I) was eluted with acids, and then the titanium-type lithium ion-sieves or adsorbents ($Li_4Ti_5O_{12}$,

* Corresponding author.
** Corresponding author.
*E-mail addresses:* wuqian0516@163.com (Q. Wu), nieezhen518@163.com (Z. Nie).

https://doi.org/10.1016/j.polymertesting.2022.107647
Received 7 January 2022; Received in revised form 4 May 2022; Accepted 23 May 2022
Available online 5 June 2022

$Li_2TiO_3$, $TiO_2$@CNT, and so on) were obtained. The adsorbent exhibits a stable structure, low dissolution-loss rate of titanium, and favourable recovery performance, which selectively adsorb Li(I) from salt-lake brine containing high-concentration Mg(II) with the maximum adsorption capacity of 49.9 mg/g [39–42]. λ-$MnO_2$ with spinel structures of the manganic oxides features three-dimensional (3-d) network-like ion channels, and Li(I) is more readily embedded in it to form a more ordered crystalline structure, which confers a special adsorption effect on Li(I) [43]. Zhang et al. prepared $HMn_2O_4$ particles with an average diameter of 20 nm, which selectively adsorbed Li(I) from the salt-lake brine. According to the distribution coefficient $K_d$, the ions are listed in descending order as Li(I), Mg(II), Ca(II), K(I), and Na(I) in the mixed solution of multiple metal ions with a pH of 10.1 [44]. Xiao et al. synthesized granular PVC- $H_4Mn_5O_{12}$ composite materials with a diameter of 2–3.5 mm using an anti-solvent method by employing polyvinyl chloride (PVC) as the binder and N-methyl pyrrolidone (NMP) as the solvent. Li(I) diffused inside the adsorbents, and the mass transfer coefficient was $K_f = (1.8–2.5) \times 10^{-5}$ m/s [45]. To improve the adsorption rate of the adsorbing materials, scholars conducted a template polymerization of high internal-phase emulsions (HIPEs) to form porous polymer PolyHIPEs. PolyHIPEs were then used as the carrier, and crown ether with specific adsorption effects on Li(I) was anchored. Therefore, a composite adsorbent was prepared, which reached an adsorption equilibrium within 2.5 h, and the adsorption kinetics agreed with the pseudo-second-order model in adsorption [46]. However, these adsorbing materials are commonly granular, which will be dissolved and lost in the process of recovering Li(I). In view of this, this study attempts to develop a high-efficient adsorbing material, which is characterized by low flow resistance, easy recovery, low cost, and no reduction in the selectivity of Li(I).

Developed from molecular imprinting technology, ion imprinting technology is an effective method to prepare adsorption materials with specific selectivity for target ions, because the adsorption vacancy formed in this way is highly matched with the charge number, radius and spatial structure of template ions [47]. The polymers prepared by ion imprinting technology show good selectivity to target ions, and surface imprinting technology can solve the problem of slow adsorption rate of the prepared materials to target ions to a great extent. Nevertheless, there still exist two problems hindering the development of ion imprinting technology for lithium extraction from salt lake. One problem is the high cost of functional units. At present, most of the ion imprinting technologies for lithium extraction reported in the literature select expensive crown ether as the functional monomer [48,49]. In the preparation of ion-imprinted polymers, since functional monomers will directly affect the recognition ability and adsorption performance of the prepared imprinted materials for target ions, the selection of functional monomers is particularly critical. Ion imprinting technology is developed from molecular imprinting technology. In the preparation of molecularly imprinted polymers, methacrylic acid is usually applied as a functional monomer, and hydrogen bonds are formed by H in the carboxyl group and N, O and other elements in the template molecule. However, there is no such general rule in the preparation of ion-imprinted polymers [50]. Another problem is the water solubility of functional monomers. The first step in the preparation of ion-imprinted polymers is the formation of complexes by the coordination of functional monomers with template ions. During this process, it is expected that as many functional monomers as possible coordinate with the template ions, thereby forming more imprinted holes. In practice, however, functional monomers (usually organic molecules) tend to have poor water solubility in aqueous solutions containing template ions [51]. This is also one of the main reasons why the currently prepared ion-imprinted polymers have poor adsorption effect on target ions. In terms of it, some researchers have proposed the use of emulsion polymerization or suspension polymerization to solve the problem of water solubility of functional monomers, but the effect is still unsatisfactory. Therefore, in the preparation of this new type of ion-imprinted material in this study, the functional groups were first grafted to the surface of the matrix material, and then the template ions were adsorbed, and the structure was fixed by polymerization. Finally, the template ions were removed by elution, that is, multiple adsorption vacancies matching the spatial structure, radius and charge number of the template ions were formed on the surface of the matrix material, solving the problem of poor water solubility of functional monomers. Selective separation of Li (I) from salt lakes by applying vinyl phosphoric acid as a functional monomer is rarely reported. In this study, electrostatic spinning technology and surface ion imprinting technology were combined to prepare a high-performance and low-cost adsorption material, which was utilized for selective separation and recovery of Li(I) in real salt lake brine.

The mobility and selectivity of the adsorbing materials are critical for the adsorption of Li(I) from the salt lakes. Based on the previous work, a new type of nanofiber material with low cost, high mobility, and stable structure was synthesized by combining the surface ion imprinting technology and high-voltage electrospinning technology. The adsorption mechanism was revealed through the characterization, adsorption experiments, and theoretical calculation of the prepared adsorbing material. The results showed that the material can be applied to separate Li(I) selectively from the salt-lake brine.

## 2. Materials and methods

### 2.1. Materials and chemicals

The salt-lake brine was collected from the carbonate-type Zabuye Salt Lake in Tibet Autonomous Region of China. The concentrations of various elements were measured by an inductively coupled plasma-atomic emission spectrometry (ICP-AES) method, and the pH value of the brine at the sampling site was 8.6. The chemical reagents for preparing the adsorbing material were purchased from Rhawn Reagent Co., Ltd and Sinopharm Chemical Reagent Co., Ltd. The chemical reagents and concentrations of the metal ions in the brine are listed in Supporting Information (Text S1 and Table S1).

### 2.2. Synthesis of the adsorbing material

5.0 mg of chromatographic silica gel (SG) were weighed and placed in a 250-mL of three-necked flask, in which 6 mol/L hydrochloric acid (HCl) was added. After reflux heating for 6 h during stirring, the solution was filtered and then washed to neutral with deionised water, followed by drying to a constant weight at 100 °C. 2.0 g of activated SG was weighed and poured in a 50 mL of three-necked flask, in which 30 mL methylbenzene was added to homogeneously disperse the activated SG. Afterwards, 2 mL of N-(2-aminoethyl)-3-aminopropyltriethoxysilane (KH-791) was added to the solution during stirring, and then 2 mL of aniline was added. The solution was heated by reflux for 15–24 h during stirring. Graphene oxide (GO) (0.068 g) and dicyclohexylcarbodiimide (DCC) (1.0 g) were added to 30 mL of N,N dimethylformamide (DMF). After dissolution, 2 g of N,N dimethylformamide (DMF) was added and reacted for 24 h at 60 °C to obtain SG/GO composites. 2.0 g of SG/GO was weighed, in which 30 of mL methylbenzene, 2 mL of KH-791, and 2 mL of aniline were added, the mixture was then heated evenly under reflux for 15–24 h, and the amino component was grafted. Maleic anhydride and glacial acetic acid were used to partially modify the double bonds on the amino-functionalised SG/GO, and 4 mL of vinylphosphonic acid were added to modify phosphoryl groups. 2.0 g of the resulting products were weighed and added to the saturated LiCl solution, then filtered and dried after 6 h. Thereafter, 30 mL of acetonitrile was added to disperse the products, followed by 2 mL of ethylene glycol dimethacrylate (EGDMA) and 150 mg of azodiisobutyronitrile. After adding stirring magnetons into the solution, $N_2$ was injected to replace air from the flask for 20 min to ensure that the whole system reacted in an oxygen-free environment. After being sealed, the flask was heated in an oil bath at 60 °Cand stirred for 24 h, and the solution was then filtered.

The polymerization was completed when the products were dried to a constant weight at 50 °C in a vacuum. The polymerization products were then eluted with 2 mol/L HCl to obtain Li(I) ion-imprinted polymer (IIP) @SG/GO containing imprinting cavities for Li(I). IIP@SG/GO nanopowders (0.5 g), DMF, and PAN fibers were poured into a three-necked flask, and then stirred magnetically for 4 h at 90 °C to prepare a transparent, homogeneous spinning solution (13 wt%). The high-voltage electrospinning was conducted at a voltage of 15 kV, a flow rate of 0.25 mL/min of spinning solution, and a rate of rotation of 450 rpm in the drum receiver. The electrospinning products were placed in a dryer to be dried at 50 °C under vacuum for 12 h. In this way, the PAN-IIP@SG/GO nanofibers were obtained. The synthesis route is illustrated in Fig. 1.

As a comparison, non-imprinted adsorbent materials were prepared through the same steps as above without immersing in the saturated LiCl solution, which was marked as PAN-Non- IIP@SG/GO nanofibers.

### 2.3. Sample characterization

A series of techniques, including scanning electron microscopy (SEM), Fourier transform infrared spectroscopy (FT-IR), X-ray photoelectron spectroscopy (XPS), and a surface area and porosity analyser were employed to test and analyse each stage in the synthesis of PAN-IIP@SG/GO and changes of PAN-IIP@SG/GO before and after adsorbing Li(I). The concentrations of each metal ion in the solution were measured by the ICP-AES method. The specifications and parameters of the test devices used are given in Supporting Information (Text S2).

### 2.4. Adsorption experiments

The static adsorption and fixed-bed adsorption experiments were conducted to investigate the adsorption performance of PAN-IIP@SG/GO. The solution was prepared with pure chemical reagents, and its pH was adjusted using dilute HCl and ammonia water. The adsorption kinetics and adsorption isotherms of PAN-IIP@SG/GO for Li(I) as well as the influences of pH on the adsorption capacity for Li(I) were investigated through the static experiments. The recycling performance and desorption ability of the adsorbing materials for Li(I) were analysed by fixed-bed adsorption experiments. A series of experiments were performed on the adsorption performance and conditions of PAN-IIP@SG/GO for the ions in the salt-lake brine. Detailed information about experiments is available in Supporting Information (Text S3).

### 2.5. Methods of calculation

Density functional theory (DFT) is used to describe the state and properties of electron density, which is one of the theoretical calculation methods in quantum chemical computation [52,53]. Due to the reliability of the B3LYP hybrid functional in processing electronic exchange and correlation in a wide range of molecular systems, the 6-31+G(d, p) basis sets therein were adopted to optimise the initial structure of the compound of PAN-IIP@SG/GO and Li(I) [54–56]. Using the Gaussian 09 software package, the adsorption mechanism of PAN-IIP@SG/GO for Li (I) was further explained by combining the DFT and a series of characterization results. The mechanism of action between PAN-IIP@SG/GO and Li(I) was revealed by calculating the natural bond orbit (NBO) of the compound. The specific calculation models are given in Supporting Information (Text S4).

## 3. Results and discussion

### 3.1. Characterization of PAN-IIP@SG/GO

Fig. 2 illustrates the SEM images of PAN-IIP@SG/GO before and after adsorbing Li(I). Fig. 2(a) demonstrates that the nanofibers have regular appearance and smooth surfaces, with many voids distributed between them. these impart lower flow resistance and excellent permeability to PAN-IIP@SG/GO in the salt-lake brine, which are beneficial toits adsorption of Li(I). It can be clearly observed from Fig. 2(b) that large numbers of particles were attached to the surface of PAN-IIP@SG/GO and even intercalated between the nanofibers, indicated that the adsorption of Li(I).

Fig. 3 displays FT-IR spectra of the activated SG and IIP@SG/GO before and after adsorbing Li(I). There were characteristic absorption peaks at 960 $cm^{-1}$, which was attributed to the scissoring vibration of Si–OH of SG. Compared with the activated SG, the intensity of the absorption peak in IIP@SG/GO at 960 $cm^{-1}$ was significantly weakened, indicating that the surfaces of SG were partly occupied and –OH on the surface underwent grafting reaction [57,58]. In Fig. 3(b), the peak at about 1734 $cm^{-1}$ corresponded to the characteristic absorption peak of –C(O)OH in EGDMA, and that at 1091 $cm^{-1}$ was assigned to the characteristic absorption peak of P–OH, which implied that vinylphosphonic acid participated in the synthesis of IIP@SG/GO. Whereas, there was no characteristic absorption peak at 1640 $cm^{-1}$, suggesting that unsaturated bonds were completely polymerized in the synthesis process [59,60]. The absorption peaks in Fig. 3(b–c) resembled each other, which showed that the Li(I) adsorption and elution processes of IIP@SG/GO did not influence the structure of the adsorbing material.

### 3.2. Adsorption behaviours

As shown in Supporting Information (Fig. S1), the adsorption capacity of Li(I) by PAN-IIP@SG/GO (0.95 mg/g) is significantly higher than that by PAN-Non-IIP@SG/GO (0.13 mg/g) under the same conditions. Therefore, in the subsequent study, we focus on the Li(I) adsorption behavior, selectivity and mechanism of PAN-IIP@SG/GO.

The pH value is one of the important factors affecting the form of the metal ions and the charge distribution on the surface of the adsorbing material, thus affecting the adsorption process. Fig. 4 shows the adsorption of PAN-IIP@SG/GO for Li(I) when the pH was between 5 and 10. The adsorption capacity of PAN-IIP@SG/GO for Li(I) was too low to be ignored when the pH was less than 5. The functional groups of PAN-IIP@SG/GO were remarkably protonated in the highly acid solution, and numerous $H^+$ in the solution with a pH lower than 5 competed with

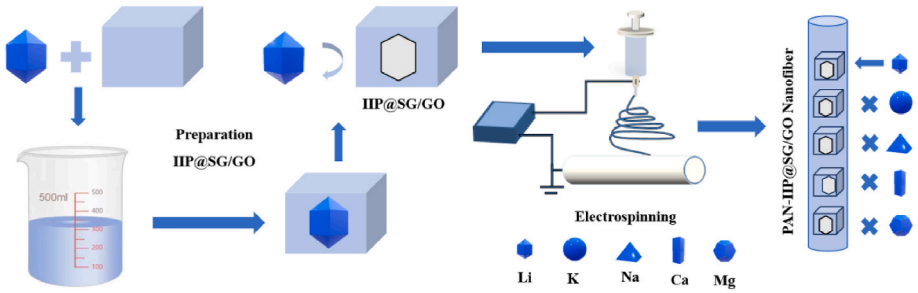


**Fig. 1.** Synthesis route of PAN-IIP@SG/GO nanofibers.

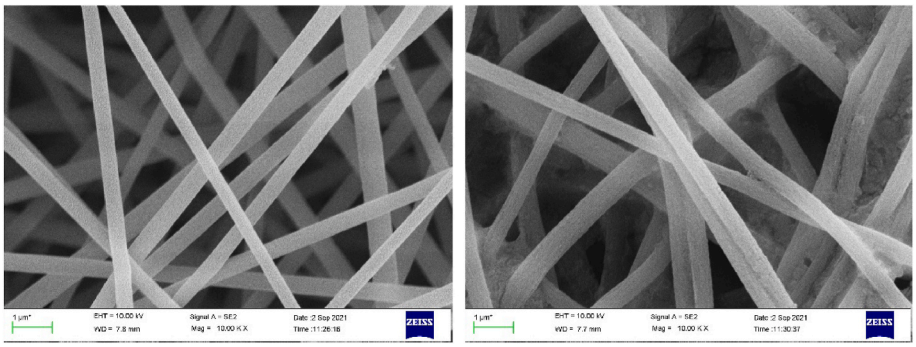

**Fig. 2.** SEM images of PAN-IIP@SG/GO before and after adsorbing Li(I).

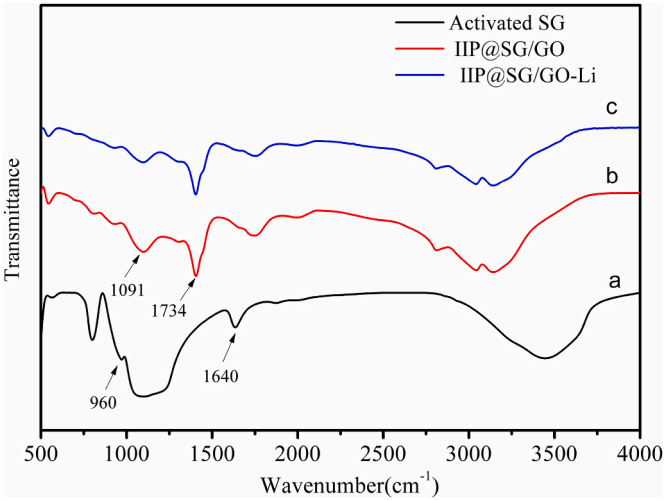


**Fig. 3.** IF spectra of activated SG (a), IIP@SG/GO before adsorbing Li(I) (b), and IIP@SG/GO after adsorbing Li(I) (c).

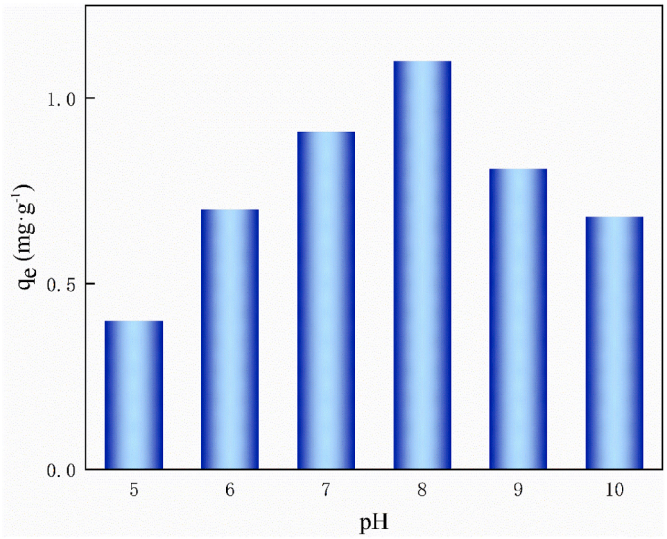


**Fig. 4.** Adsorption capacities of PAN-IIP@SG/GO for Li(I) within a pH range of 5–10.

Li(I) for coordination with functional groups. The adsorption capacity of PAN-IIP@SG/GO gradually increased in the solution with pH values of 5–8. The adsorption capacity reached the maximum of 1.1 mg/g as the pH increased to 8 (the subsequent experiments were conducted at pH = 8 unless otherwise specified). The protonation weakened and the adsorption sites on PAN-IIP@SG/GO increased with the increase of pH value, and the adsorption capacity for Li(I) was also enhanced. Once the pH was greater than 8, the adsorption capacity began to decrease. The quantity of $OH^-$ increased in the alkaline solution, leading to the decrease in the adsorption capacity of PAN-IIP@SG/GO for Li(I) (In Supporting Information Fig. S2).

Fig. S3 illustrates the changes in the adsorption capacity of PAN-IIP@SG/GO for Li(I) with time. The whole adsorption process experienced rapid adsorption, slow adsorption, and adsorption equilibrium. The adsorption capacity increased rapidly in the first 90 min, then increased slowly, and remained quasi-constant from about 120 min, indicating that it reached adsorption equilibrium. There was a large amount of Li(I) in the initial solution, and PAN-IIP@SG/GO contained numerous effective adsorption sites, which promoted PAN-IIP@SG/GO capture Li(I) in the solution. After a period of adsorption, the concentration of Li(I) decreased, the driving force of the mass transfer increased, and the original adsorption sites of PAN-IIP@SG/GO were also constantly occupied. Consequently, the adsorption rate decreased after 90 min, and it took a long time to reach adsorption equilibrium. Nevertheless, the adsorption rate of the prepared adsorbing material was still much greater than that of other materials mentioned in previous research (Table 1), indicating that the adsorption sites of acidic functional monomers prepared by surface imprinting were easier to capture Li(I). Therefore, PAN-IIP@SG/GO exhibited potential for industrial application.

The adsorption mechanism of PAN-IIP@SG/GO for Li(I) was further revealed from the macroscopic perspective. The pseudo-first-order and pseudo-second-order models were used to fit the data in the kinetics experiments (Supporting Information, Fig. S4), and the relevant data are listed in Table 2. According to the fitting results of kinetics models, the correlation coefficient of the pseudo-second-order model ($R_2^2 = 0.991$) was greater than that of the pseudo-first-order model ($R_1^2 = 0.967$). In addition, the adsorption capacity obtained by the pseudo second-order model was close to the experimental data. Therefore, the adsorption of PAN-IIP@SG/GO for Li(I) can be described by using the pseudo-second-order model, and the adsorption process was regarded as chemical adsorption.

The adsorption fitting curves of PAN-IIP@SG/GO for Li(I) with Freundlich and Langmuir adsorption isotherm models are illustrated in Fig. 5, and the relevant fitting data are listed in Table 3. As shown in

**Table 1**
Adsorption performance of Li(I) adsorbents in the literature.

| Types of adsorbents | Time to adsorption equilibrium (h) | Reference |
|---|---|---|
| HTO | 30 | [61] |
| HTO-ceramic foams | 24 | [62] |
| Li/Al-LDHs | 24 | [63] |
| $MnO_2{\cdot}0.5H_2O$ | 12.5 | [64] |
| PAN-IIP@SG/GO | 2 | This research |

**Table 2**
Reaction kinetic parameters.

| Temperature (K) | Pseudo-first-order | | | Pseudo-second-order | | |
|---|---|---|---|---|---|---|
| 298 | $k_1$(min$^{-1}$) | $q_{e,cal}$(mg/g) | $R_1^2$ | $k_2$(mg/(g·min)) | $q_{e,cal}$(mg/g) | $R_2^2$ |
| | 0.059 | 0.43 | 0.967 | 0.026 | 0.50 | 0.991 |

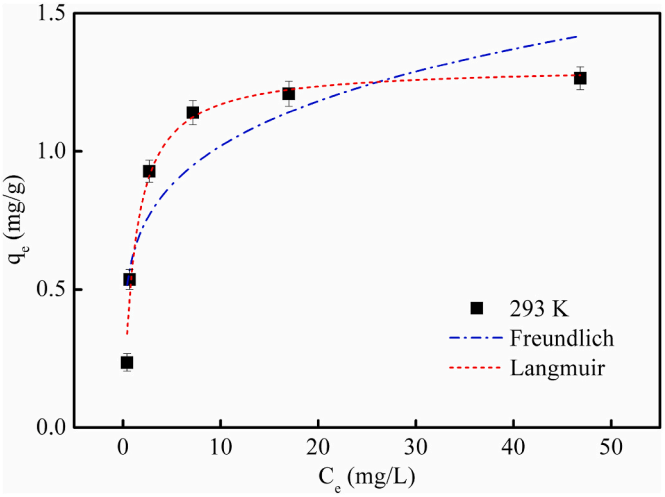


**Fig. 5.** Comparisons of Langmuir and Freundlich adsorption models for Li(I) adsorption by the adsorbing material.

**Table 3**
Parameters of Langmuir and Freundlich models.

| Temperature (K) | Langmuir | | | Freundlich | | |
|---|---|---|---|---|---|---|
| | $q_{max,cal}$ (mg/g) | $K_L$ (L/mg) | $R_L^2$ | n | $K_F$ (mg/g) | $R_F^2$ |
| 298 | 1.31 | 1.307 | 0.977 | 4.889 | 0.624 | 0.754 |

Table 3, the Langmuir adsorption model was more applicable in describing the adsorption process. The adsorption capacity calculated by the Langmuir model was closer to the experimental data, and the correlation coefficient of the Langmuir adsorption model ($R_L^2 = 0.977$) was larger than that of the Freundlich adsorption model ($R_F^2 = 0.754$). The fitting curve of the Langmuir adsorption model indicated that the adsorption capacity increased rapidly at first and then increased slowly with the increase of the Li(I) concentration in the solution. The adsorption capacity remained unchanged after the adsorption was saturated. The adsorption of PAN-IIP@SG/GO for Li(I) was mainly dependent on the complexation of the functional monomers with Li(I), and Li(I) was eluted to produce identification sites for Li(I). The number of effective adsorption sites in PAN-IIP@SG/GO is finite. In the initial period, the driving force of the mass transfer constantly increased with the increase of the Li(I) concentration. In this case, there were abundant adsorption sites in PAN-IIP@SG/GO, which increased the adsorption capacity rapidly. After occupying effective adsorption sites in PAN-IIP@SG/GO, the adsorption capacity remained unchanged even though the concentration of Li(I) increased. Therefore, it was deemed that there were a finite number of effective adsorption sites in PAN-IIP@SG/GO, the adsorption process was one of monolayer adsorption, and the nanofibers themselves did not interact.

### 3.3. Selectivity and recycling performance

To evaluate whether the material can be further applied in industry, the adsorption selectivity of PAN-IIP@SG/GO was tested under different pH values. The actual brine used in the research contained metal cations associated with Li(I), including Na(I), K(I), Mg(II), and Ca(II), the five metal ions were added to the solution to explore the adsorption selectivity of PAN-IIP@SG/GO. The solutions with pH values of 6, 8, and 10 were prepared to investigate the adsorption selectivity of PAN-IIP@SG/GO. The selective adsorption data are listed in Table 4. Table 4 showed that PAN-IIP@SG/GO had high selectivity for Li(I), while a certain amount of Mg(II) was also adsorbed, which was due to the similar radius of Mg(II) (0.065 nm) with Li(I) (0.068 nm). For the desorption of PAN-IIP@SG/GO, 1 M HCl was used. After five cyclic adsorption-desorption experiments, the adsorption capacity of PAN-IIP@SG/GO was only reduced by 10.91%, which indicated that the material can be recycled (Fig. 6).

### 3.4. Adsorption mechanism

Fig. 2 shows the SEM images of PAN-IIP@SG/GO. The PAN-IIP@SG/GO nanofibers after adsorption in Fig. 2(b) were 1.5–2 times thicker than those in Fig. 2(a) before adsorption. the surface of the PAN-IIP@SG/GO nanofiber became rough after adsorption, and many particles were adsorbed thereon. P–O and P═O in the functional monomers were complexed with Li(I), and the locations of the P and O atoms in the adsorption sites were changed, leading to the thickening of nanofibers. The comparison of IF spectra of PAN-IIP@SG/GO before and after adsorption showed that the characteristic absorption peak of –C(O)OH in EGDMA originally at 1734 cm$^{-1}$ and that of P–OH at 1091 cm$^{-1}$ both shifted to the low frequency after adsorption, which implies that the functional groups were complexed with Li(I). Fig. 7 illustrates the XPS fitting curves of PAN-IIP@SG/GO before and after adsorbing Li(I). There was no characteristic peak attributed to Li(I) in the full-spectrum fitting curve in Fig. 7(a), while a new characteristic peak occurred at 55.9 eV after adsorption [65], which was attributed to Li(I) coordinated with P–O. In Fig. 7(b), the characteristic peaks of P–O and P═O before adsorption were separately located at 530.61 and 531.62 eV [66], which were shifted to 530.74 and 531.73 eV after adsorption. In Fig. 7(c), the characteristic peak attributed to P shifted from 133.80 eV to 133.95 eV after adsorption, which was due to the participation of P–O, P═O, and P (as the electron donors) in the adsorption of Li(I).

DFT was used to elucidate the interaction mechanism between the functional groups of the adsorbent and the Li(I). Fig. 8 shows the optimal structures of the surface functional groups before and after combining with Li(I), and the relevant calculation parameters are listed in Table 5. The electrostatic potentials of the functional groups on the surface of the adsorbent (Fig. 8(a)) and the optimised geometry after combining with

**Table 4**
Selective adsorption parameters of PAN-IIP@SG/GO.

| Ions | pH | Distribution coefficient ($K_d$) (ml/g) | | Selectivity coefficient ($K$) |
|---|---|---|---|---|
| | | D (*Li*) | D (*M*) | |
| Li(I)/Mg(II) | 6 | 14.20 | 1.16 | 12.24 |
| | 8 | 22.49 | 2.00 | 11.25 |
| | 10 | 13.79 | 2.20 | 6.27 |
| Li(I)/Na(I) | 6 | 13.99 | 0.26 | 53.81 |
| | 8 | 22.29 | 0.44 | 50.66 |
| | 10 | 13.81 | 0.38 | 36.34 |
| Li(I)/K(I) | 6 | 14.40 | 0.16 | 90.00 |
| | 8 | 22.91 | 0.20 | 114.55 |
| | 10 | 14.61 | 0.18 | 81.17 |
| Li(I)/Ca(II) | 6 | 14.82 | 0.22 | 67.36 |
| | 8 | 24.38 | 0.84 | 29.02 |
| | 10 | 13.58 | 1.00 | 13.58 |

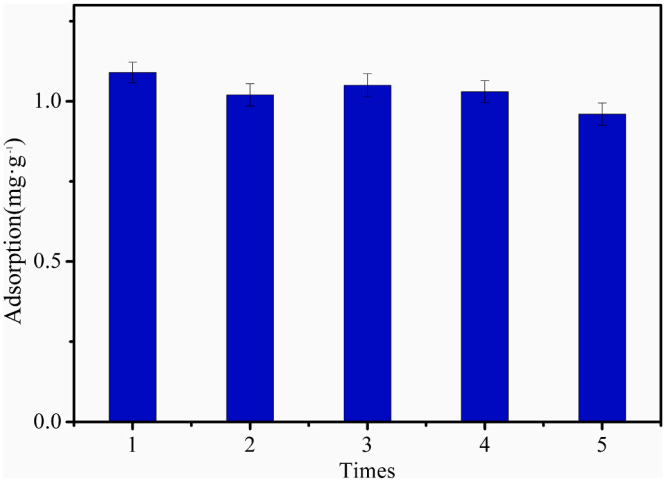


**Fig. 6.** Recycling performance.

Li(I) (Fig. 8(b)) were ascertained. On this basis, it was preliminarily inferred that –(PO)$(OH)_2$ is the key adsorption site for the binding of adsorbent with Li(I). The bond lengths of P–Li and O–Li were 3.68 Å, 3.19 Å, 3.29 Å, and 4.19 Å, and the adsorption energy was −96.04 kJ/mol, indicating that the adsorption of the PAN-IIP@SG/GO adsorbent for Li(I) was classified as stable chemical adsorption. The specific mechanism of action was further studied via the NBO. The NBO analysis of partial charges showed that the charge of Li(I) was 0.98, while that of its ligand was 0.02, suggesting the charge transfer between the surface functional group and metal ion during the adsorption. The natural electron configuration of Li(I) was shown as $2s^{0.02}3p^{0.15}$, which indicated that the electrons were mainly transferred from the functional groups to the 3p orbit of Li(I).

Fig. 9 illustrates the comparison of the highest occupied molecular orbitals (HOMOs) and lowest unoccupied molecular orbitals (LUMOs) of PAN-IIP@SG/GO before and after adsorbing Li(I). The HOMOs of PAN-IIP@SG/GO before adsorbing Li(I) were mainly distributed on the C and H atoms, while they were mainly found on the -(PO)$(OH)_2$ functional group and Li(I) after adsorption. The LUMOs of PAN-IIP@SG/GO before adsorbing Li(I) were mainly located at the -(PO)$(OH)_2$ functional group, while they were mainly on Li, P, and O atoms after adsorption. This phenomenon further proved the electron transfer between the ligand and the metal ions in the adsorption process. The stabilization energy *E* (2) reflected the extent of electron transfer from the HOMOs to LUMOs. Therefore, the electron transfer between -(PO)$(OH)_2$ and Li(I) was explored by calculating the second-order perturbation energy, and the results are listed in Table 5. The stabilization energy *E*(2) of LP(P)-LP*(In) and LP(O)-LP*(In) of Li(I) was 3.43, 4.23, 3.01, and 2.22 kJ/mol, which further verified that PAN-IIP@SG/GO reached the goal of adsorbing Li(I) by forming coordinated bonds with Li(I) mainly using the P and O atoms of the functional groups.

### 3.5. Practical applications in salt-lake

In order to investigate the practical applications of the Li(I) adsorption capacity of PAN-IIP@SG/GO, the PAN-IIP@SG/GO was used to adsorb the Li(I) in the actual salt lake. The chemical composition of the salt-lake is shown in Table S1, and the amount of salt-lake brine was controlled to 200 mL per portion. Fig. S5 shows the variation of the Li(I), Na(I), K(I), Mg(II), and Ca(II) concentrations in the salt-lake brine for different adsorbent additions. The adsorption rate for Li(I) in the salt-lake brine increased gradually and changed significantly as the adsorbent increased, while the concentrations of Na(I), K(I), Mg(II), and Ca(II) ions also increased to some extent, which indicated that the adsorbent had a certain adsorption capacity and selectivity for Li(I) in the salt lake. The results indicated that the adsorbent had the potential for application.

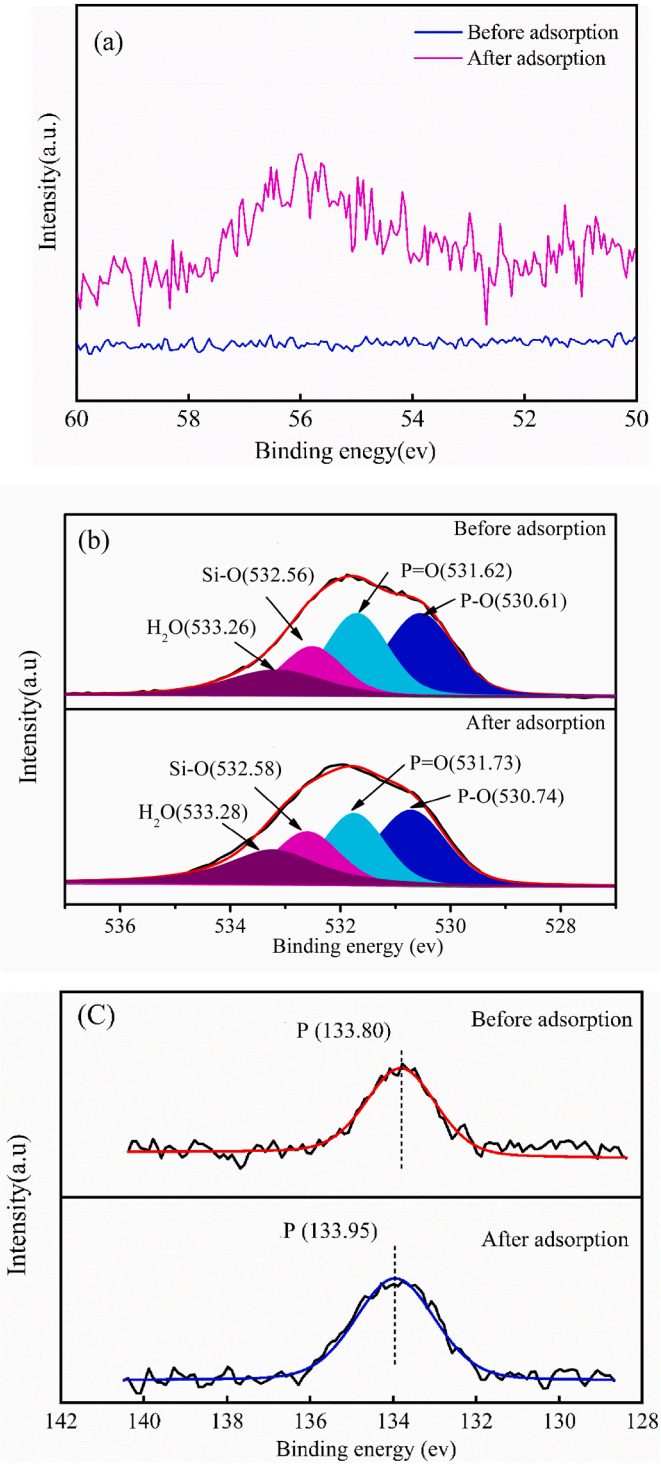


**Fig. 7.** XPS fitting curves of PAN-IIP@SG/GO before and after Li(I) adsorption.

## 4. Conclusion

PAN-IIP@SG/GO nanofiber was prepared by combining ion-imprinting technique and electrospinning for directional capturing Li(I) from the salt-lake brine. PAN-IIP@SG/GO exhibited a favourable selectivity for Li(I), and the adsorption capacity was only decreased by 10.91% after five adsorption-desorption cycles. The adsorption reached

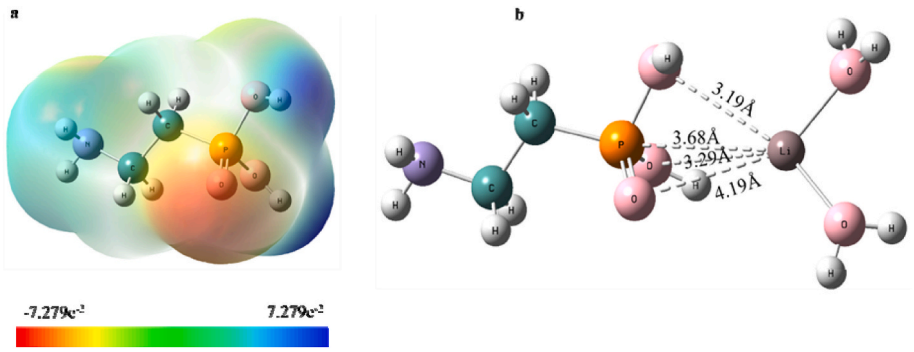


**Fig. 8.** (a) The optimised geometry and electrostatic potential analysis of functional groups, and (b) the optimised geometry of complexes.

**Table 5**
Calculated parameters for the complex.

| Complex | Interaction energy (kJ/mol) | NBO partial charge | | M(I) electron configuration | *E*(2) Energy ((kJ/mol) | | | |
|---|---|---|---|---|---|---|---|---|
| | | Ligand | M(I) | | LP(P10)-LP*(M) | LP(O11)-LP*(M) | LP(O12)- LP*(M) | LP (014)- LP*(M) |
| Li(I) complex | −96.04 | 0.02 | 0.98 | $2s^{0.02}3p^{0.15}$ | 3.43 | 4.23 | 3.01 | 2.22 |

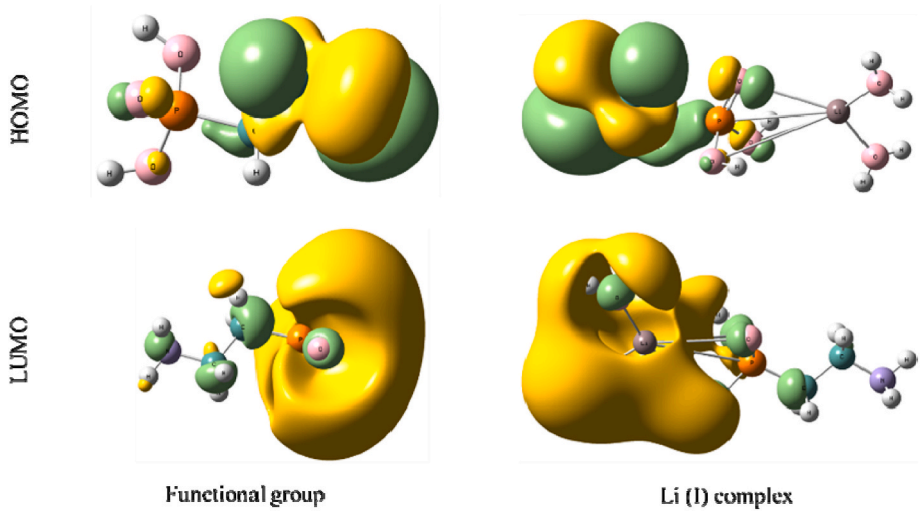


**Fig. 9.** The contour plots of HOMOs and LUMOs of functional groups and the corresponding complexes.

equilibrium within 120 min, and the maximum adsorption capacity for Li(I) was 1.1 mg/g. The fitting results showed that the adsorption was governed by the Langmuir adsorption isothermal model, and the adsorption kinetics followed the pseudo-second-order model. The adsorption is monolayer chemical adsorption, and the adsorbing material itself did not undergo a chemical reaction. In addition, the adsorption mechanism of PAN-IIP@SG/GO for Li(I) was revealed by a series of characterization, adsorption experiments, and DFT computation. The P and O atoms of the functional groups form coordinated bonds with Li(I) and electrons mainly were transferred from the functional groups to the 3p orbit of Li(I), thus realizing the capture of Li(I). PAN-IIP@SG/GO was proved to be an effective adsorbing material for directional capturing Li (I) in the salt lakes and exhibited promising industrial application prospects.

## Author statement

**Tao Ding**: Investigation, Data curation, Formal analysis, Writing-original draft, Writing-review & editing. **Qian Wu** and **Zhen Nie**: conception, outline, major write up, and review. **Mianping Zheng and Yunsheng Wang**: critical review, content suggestions, and proof-reading. **Donghui Yang:** Data curation, Formal analysis.

## Declaration of competing interest

The authors declare that they have no known competing financial interests or personal relationships that could have appeared to influence the work reported in this paper.

## Acknowledgments

The authors gratefully thank the National Natural Science Foundation of China for financial support (U20A20148).

## Appendix A. Supplementary data

Supplementary data to this article can be found online at https://doi.org/10.1016/j.polymertesting.2022.107647.

## References


[1] M. Wisniewska, et al., Investigations of the possibility of lithium acquisition from geothermal water using natural and synthetic zeolites applying poly(acrylic acid), J. Clean. Prod. 195 (2018) 821–830.
[2] J. Qian, et al., High rate and stable cycling of lithium metal anode, Nat. Commun. 6 (2015) 6362.
[3] X. Li, et al., Membrane-based technologies for lithium recovery from water lithium resources: a review, J. Membr. Sci. 591 (2019), 117317.
[4] T. Zhao, et al., High-performance, reaction sintered lithium disilicate glass-ceramics, Ceram. Int. 40 (8) (2014) 12449–12457.
[5] R.H. Cyburt, et al., Nuclear reaction uncertainties, massive gravitino decays and the cosmological lithium problem, J. Cosmol. Astropart. Phys. 10 (2010), 032-032.
[6] A. Schulz, et al., Quantifying lithium in the solid electrolyte interphase layer and beyond using Lithium- Nuclear Reaction Analysis technique, J. Power Sources 360 (2017) 129–135.
[7] A. Reddy, et al., Synthesis of nitrogen-doped graphene films for lithium battery application, ACS Nano 4 (11) (2010) 6337–6342.
[8] X. Tao, et al., Balancing surface adsorption and diffusion of lithium-polysulfides on nonconductive oxides for lithium–sulfur battery design, Nat. Commun. 7 (2016), 11203.
[9] K.J. Griffith, et al., Niobium tungsten oxides for high-rate lithium-ion energy storage, Nature 559 (7715) (2018) 556–563.
[10] Y. Qiao, et al., Toxicity analysis of second use lithium-ion battery separator and electrolyte, Polym. Test. 81 (2019), 106175.
[11] G. Martin, et al., Lithium market research-global supply, future demand and price development, Energy Storage Mater. 6 (2017) 171–179.
[12] G. Liu, et al., Novel approaches for lithium extraction from salt-lake brines: a review, Hydrometallurgy 187 (2019) 81–100.
[13] X. Xu, et al., Extraction of lithium with functionalized lithium ion-sieves, Prog. Mater. Sci. 84 (2016) 276–313.
[14] J. Yu, et al., Lithium extraction from carbonate-type saline lake by utilizing of geothermal solar pond in Tibet, Acta Geol Sin-Engl. 88 (supp. 1) (2014) 389–390.
[15] Z. Nie, et al., Phase chemistry study of the dangxiongcuo salt lake brine: isothermal evaporation at 25°C, Acta Geol Sin-Engl. 88 (supp. 1) (2014) 361–362.
[16] Z. Nie, et al., Phase chemistry study on brine from the Zabuye carbonate-type salt lake in Tibet, Acta Geol Sin-Engl. 84 (4) (2010) 587–592.
[17] Z. Nie, et al., Experimental study of the Tibetan Dangxiong Co salt lake brine during isothermal evaporation at 25 °C, Carbonates Evaporites 35 (1) (2020).
[18] T. Ding, et al., Polyacrylonitrile/crown ether composite nanofibres with high efficiency for adsorbing Li(I): experiments and theoretical calculations, Front. Energy Res. 9 (2021), 765612.
[19] Z. Nie, et al., Experimental study of natural brine solar ponds in Tibet, Sol. Energy 85 (7) (2011) 1537–1542.
[20] Z. Ye, et al., Lithium extraction from water lithium resources through green electrochemical-battery approaches: a comprehensive review, J. Clean. Prod. 285 (2020), 124905, https://doi.org/10.1016/j.jclepro.2020.124905. In press.
[21] B. Swain, Recovery and recycling of lithium: a review, Separ. Purif. Technol. 172 (2017) 388–403.
[22] F. Meng, et al., Review of lithium production and recovery from minerals, brines, and lithium-ion batteries, Miner. Process. Extr. Metall. (IMM Trans. Sect. C) 42 (2019) 1–19.
[23] P.K. Choubey, et al., Advance review on the exploitation of the prominent energy-storage element Lithium. Part II: from sea water and spent lithium ion batteries (LIBs), Miner. Eng. 110 (2017) 104–121.
[24] D. Shi, et al., Lithium extraction from low-grade salt lake brine with ultrahigh Mg/Li ratio using TBP- kerosene- $FeCl_3$ system, Separ. Purif. Technol. 211 (2018) 303–309.
[25] C. Shi, et al., Solvent extraction of lithium ions by tri-n-butyl phosphate using a room temperature ionic liquid, J. Mol. Liq. 215 (2016) 640–646.
[26] W. Zhou, et al., Extraction of lithium from magnesium-rich solution using tri-n-butyl phosphate and sodium hexafluorophosphate, J Sustain Metall 7 (3) (2021) 1368–1378.
[27] A. Razmjou, et al., Design principles of ion selective nanostructured membranes for the extraction of lithium ions, Nat. Commun. 10 (2019).
[28] H. Saravaia, et al., Sulfonated poly (ether ether ketone) composite cation exchange membrane for selective recovery of lithium by electrodialysis, Desalination 496 (2020), 114755.
[29] K.S. Chung, et al., Inorganic adsorbent containing polymeric membrane reservoir for the recovery of lithium from seawater, J. Membr. Sci. 325 (2) (2008) 503–508.
[30] S. Xu, et al., Extraction of lithium from Chinese salt-lake brines by membranes: design and practice, J. Membr. Sci. 635 (2021), 119441.
[31] Z. Li, et al., Continuous electrical pumping membrane process for seawater lithium mining, Energy Environ. Sci. 14 (2021) 3152–3159.
[32] B.K. Pramanik, et al., Lithium recovery from salt-lake brine: impact of competing cations, pretreatment and preconcentration, Chemosphere 260 (2020), 127623.
[33] R. Marthi, et al., Application and limitations of a $H_2TiO_3$–Diatomaceous earth composite synthesized from titania slag as a selective lithium adsorbent, Separ. Purif. Technol. 254 (2020).
[34] H. Jiang, et al., Application of concentration-dependent HSDM to the lithium adsorption from brine in fixed bed columns, Separ. Purif. Technol. 241 (2020), 116682.
[35] B. Xla, et al., Taming wettability of lithium ion sieve via different TiO 2 precursors for effective Li recovery from aqueous lithium resources, Chem. Eng. J. 392 (2020).
[36] J.M. Jeong, et al., Effect of chemical treatments on lithium recovery process of activated carbons, J. Ind. Eng. Chem. 27 (2015) 329–333.
[37] M. Moazeni, et al., Hydrothermal synthesis and characterization of titanium dioxide nanotubes as novel lithium adsorbents, Mater. Res. Bull. 61 (2015) 70–75.
[38] Q.H. Zhang, et al., Lithium selective adsorption on lowdimensional titania nanoribbons, Chem. Eng. Sci. 65 (2010) 165–168.
[39] X. Xu, et al., Lithium adsorption performance of a three-dimensional porous $H_2TiO_3$-type lithium ion-sieve in strong alkaline Bayer liquor, RSC Adv. 7 (31) (2017) 18883–18891.
[40] L. Zhang, et al., Preparation of $H_2TiO_3$-lithium adsorbent by the solgel process and its adsorption performance, Appl. Surf. Sci. 368 (2016) 82–87.
[41] G. He, et al., The optimal condition for $H_2TiO_3$–lithium adsorbent preparation and $Li^+$ adsorption confirmed by an orthogonal test design, Ionics 21 (8) (2015) 2219–2226.
[42] D.L. Gu, et al., Lithium ion sieve synthesized via an improved solid state method and adsorption performance for West Taijinar Salt Lake brine, Chem. Eng. J. 350 (2018) 474–483.
[43] U. Kamran, S.J. Park, MnO2-decorated biochar composites of coconut shell and rice husk: an efficient lithium ions adsorption-desorption performance in aqueous media, Chemosphere 260 (2020), 127500.
[44] Q.H. Zhang, et al., $LiMn_2O_4$ spinel direct synthesis and lithium ion selective adsorption, Chem. Eng. Sci. 65 (2010) 169–173.
[45] J.L. Xiao, et al., Lithium ion recovery from brine using granulated polyacrylamide-$MnO_2$ ion-sieve, Chem. Eng. J. 279 (2015) 659–666.
[46] W. Huang, et al., 2-Methylol-12-crown-4 ether immobilized PolyHIPEs toward recovery of lithium(I), New J. Chem. 42 (2018) 16814–16822.
[47] Y. Wu, et al., Double-layer-based molecularly imprinted membranes for template-dependent recognition and separation: an imitated core-shell-based synergistic integration design, Chem. Eng. J. 397 (2020), 125371.
[48] J. Xu, et al., Simultaneous adsorption of Li (I) and Rb (I) by dual crown ethers modified magnetic ion imprinting polymers, Appl. Organomet. Chem. 33 (3) (2019) e4778.
[49] J. Lu, et al., Multilayered ion-imprinted membranes with high selectivity towards $Li^+$ based on the synergistic effect of 12-crown-4 and polyether sulfone, Appl. Surf. Sci. 427 (2018) 931–941.
[50] M. Arabi, et al., Molecular imprinting: green perspectives and strategies, Adv. Mater. 33 (2021), 2100543.
[51] Y. Wu, et al., Three-dimensional basswood-based membrane with well-designed multilevel/hierarchical imprinting surface: a high-efficiency selective separation system, Chem. Eng. J. 398 (2020), 125636.
[52] N. Schuch, et al., Computational complexity of interacting electrons and fundamental limitations of density functional theory, Nat. Rev. Phys. 5 (10) (2010) 732–735.
[53] L.C. Yin, et al., Understanding the interactions between lithium polysulfides and N-doped graphene using density functional theory calculations, Nano Energy 25 (2016) 203–210.
[54] A. Hirata, et al., Geometric frustration of icosahedron in metallic glasses, Science 341 (6144) (2013) 376–379.
[55] H. Liu, et al., The adsorption, diffusion and capacity of lithium on novel boron-doped graphene nanoribbon: a density functional theory study, Appl. Surf. Sci. 466 (2019) 737–745.
[56] N.A. Mahammedi, et al., Prediction of optically-active transitions in type-VIII guest-free silicon clathrate Si46: a comparative study of its physical properties with type-I counterpart through first-principles, J. Appl. Phys. 122 (20) (2017) 205103.1–205103.11.
[57] G. Ren, et al., Effect of MWCNTs-GO hybrids on tribological performance of hybrid PTFE/Nomex fabric/phenolic composite, Compos. Sci. Technol. 146 (2017) 155–160.
[58] Z. Li, et al., Adsorption of indium(III) from aqueous solution on raw, ultrasound- and supercritical-modified chitin: experimental and theoretical analysis, Chem. Eng. J. 373 (2019) 1247–1253.
[59] M. Li, et al., A novel nanocomposite based silica gel/graphene oxide for the selective separation and recovery of palladium from a spent industrial catalyst, Chem. Eng. J. 386 (2020), 123947.
[60] Y. Huang, et al., Thiol-ene synthesis of thioether/carboxyl-functionalized polymers for selective adsorption of silver(I) ions, Chem. Eng. J. 375 (2019), 121935.
[61] S. Wang, et al., Selective adsorption of lithium from high Mg-containing brines using $H_xTiO_3$ ion sieve, Hydrometallurgy 174 (2017) 21–28.
[62] L. Zhang, et al., Synthesis of $H_2TiO_3$–lithium adsorbent loaded on ceramic foams, Mater. Lett. 145 (2015) 351–354.
[63] Y. Sun, et al., Highly efficient extraction of lithium from salt lake brine by LiAl-layered double hydroxides as lithium-ion-selective capturing material, J. Energy Chem. 34 (2019) 80–87.
[64] G. Zhang, et al., Practical synthesis of manganese oxide $MnO_2{\cdot}0.5H_2O$ for an advanced and applicable lithium ion-sieve, J. Solid State Chem. 293 (2021), 121768.
[65] J. Zhao, et al., Experimental and DFT studies on the selective adsorption of Pd(II) from wastewater by pyromellitic-functionalized poly(glycidyl methacrylate) microsphere, J. Mol. Liq. 300 (2020), 112296.
[66] Z. Lin, et al., Investigation of phosphate removal mechanisms by a lanthanum hydroxide adsorbent using p-XRD, FTIR and XPS, Appl. Surf. Sci. 557 (2021), 149838.